nature communications

Article

https://doi.org/10.1038/s41467-026-68673-0

# Boosting carbon nanotube transistors through γ-ray irradiation

Received: 17 April 2025

Accepted: 14 January 2026

Published online: 21 January 2026

Check for updates

Ke Zhang[1,2,8], Ningfei Gao[3,4,8], Jiahao Zhang[3], Yang Li[5], Jibo Zhao[1], Daming Zhou[1], Xinhe Wang[1,2], Peng Liu[6], Xiaoyang Lin[1,2] ✉, Haitao Xu[3,4,7] ✉, Lian-Mao Peng[3,4] ✉ & Weisheng Zhao[1,2]

Advanced electronics in the post-Moore era require foundry-level performance enhancements. Carbon nanotube field-effect transistors, compatible with commercial silicon manufacturing, surpass the fundamental performance limits of silicon field-effect transistors. However, interface imperfections between carbon nanotubes and the dielectric cause poor gate controllability and current leakage. This work demonstrates that organic molecules near the carbon nanotubes can be mitigated by high-energy γ-ray irradiation. The treatment reduces off-state current density to 112.2 pA μm$^{-1}$, approaching the 100 pA μm$^{-1}$ low-power target, and achieves an on/off ratio of ~10$^5$. The quasi-gate-all-around architecture shows radiation tolerance up to 100 Mrad(Si), surpassing traditional silicon-based devices by over two orders of magnitude. This foundry-compatible strategy operates at room temperature with high throughput, advancing the practical application of nanotube transistors.

As the advantages of scaling silicon field-effect transistors (FETs) diminish[1], transistors made from nanomaterials have gained significant attention due to their short-channel immunity and low power consumption[2,3]. Carbon nanotube FETs (CNTFETs), which use semiconducting carbon nanotubes (s-CNTs) as the channel material, have exhibited superior electrical performance and power efficiency compared to silicon FETs[4–7]. Notable advancements in material processing[5,8,9], device fabrication[4,10], system-level functionality[11–14], and, most recently, successful compatibility with existing silicon manufacturing facilities[15] have positioned CNTFETs on the brink of commercialization in semiconductor foundries[16–20]. However, the imperfect interfaces between CNTs and dielectrics remain a critical challenge. Induced gap states can facilitate carrier tunneling and trapping, resulting in undesirable power consumption marked by higher off-state current density ($I_{off}$) and increased subthreshold swing (SS) values. The primary issue has been traced to organic molecules that arise during the post-synthesis separation of s-CNTs and throughout the device fabrication process. Consequently, there is an urgent need to explore techniques that can enhance CNTFET performance by addressing these organic contaminants, particularly in a manner that is compatible with foundry processes, featuring low thermal budgets, high throughput, and wafer-scale uniformity.

To enhance the quality of the CNT/dielectric interface by disrupting embedded organic materials, various forms of energy have been utilized to achieve the required bond dissociation energies (BDEs): (I) chemical energy[21] (for decomposing polymers into smaller molecules), (II) thermal energy[22] (for oxidative cracking of organics), and (III) electron-beam energy[23,24] (for bond breaking through electron kinetics). However, these methods have limitations, including specificity to certain chemical bonds, excessively high thermal budgets, and potential changes to the doping state.

In addition, these approaches often introduce new interface states, resulting in only limited improvements – or even degradation – in the $I_{off}$ and SS of CNTFETs. For successful technology transfer to

[1]Fert Beijing Institute, School of Integrated Circuit Science and Engineering, Beihang University, Beijing, China. [2]State Key Laboratory of Spintronics, Hangzhou International Innovation Institute, Beihang University, Hangzhou, China. [3]Key Laboratory for the Physics and Chemistry of Nanodevices, Center for Carbon-based Electronics, School of Electronics, Peking University, Beijing, China. [4]Beijing Institute of Carbon-based Integrated Circuits, Beijing, China. [5]Beijing Computational Science Research Center, Beijing, China. [6]State Key Laboratory of Low Dimensional Quantum Physics, Department of Physics, Tsinghua University, Beijing, China. [7]Institute of Carbon-based Thin Film Electronics, Peking University, Taiyuan, China. [8]These authors contributed equally: Ke Zhang, Ningfei Gao. ✉e-mail: XYLin@buaa.edu.cn; htxu@pku.edu.cn; lmpeng@pku.edu.cn

industry, an ideal technique should meet at least three key criteria: efficiency (high energy, deep penetration, precise controllability, and stability), performance (enhancements in electrical parameters related to interface quality, such as $I_{off}$ and SS), and manufacturability (low thermal budget, high throughput, scalability for wafer processing, and cost-effectiveness).

In this work, we propose that these requirements can be effectively fulfilled through the use of γ-ray irradiation, a technique that harnesses high-energy photons emitted from the decay of $^{60}$Co (half-life: 5.27 years)[25]. The energy of γ-rays, at 1.17 MeV and 1.33 MeV, is significantly higher than that of electron beams (approximately 10 keV) and the thermal energy associated with the annealing process (around 75 meV). Energy deposited through mechanisms such as Compton scattering typically results in permanent damage to chemical bonds, especially those with low BDEs (Supplementary Notes. 1-2, Supplementary Fig. 1). However, carbon nanotubes (CNTs), due to their nanoscale cross-sections, robust chemical bonds, and low backscattering capabilities, can endure prolonged exposure to a harsh γ-ray environment[26–28]. As a result, γ-ray irradiation can selectively disrupt organic compounds without harming the CNTs themselves. Furthermore, the power (energy per unit time) absorbed by a single CNT segment from γ-rays is substantially lower than that absorbed during thermal annealing (about $10^{-8}$ less) and electron-beam irradiation (approximately $10^{-13}$ less) (see "Methods"), indicating a high level of controllability with this approach. With improved interface quality, we achieved a reduction of 41 mV dec$^{-1}$ in SS (from 175.9 to 134.9 mV dec$^{-1}$) and a decrease of an order of magnitude in $I_{off}$. The resulting on/off ratio of $10^5$ reached the highest level among networked CNTFETs under saturated bias conditions. Moreover, this strategy offers high throughput, capable of processing over 8000 twelve-inch or 80,000 four-inch wafers per month (see Fig. 1a–c, Methods and Supplementary Fig. 2 for details). Combined with advantages such as a low thermal budget (operating at room temperature), cost-effectiveness (Supplementary Note. 3), high uniformity, and efficiency, γ-ray irradiation presents a foundry-compatible technique for CNTFET post-treatment, further paving the way for CNTFETs to become mainstream device technology.

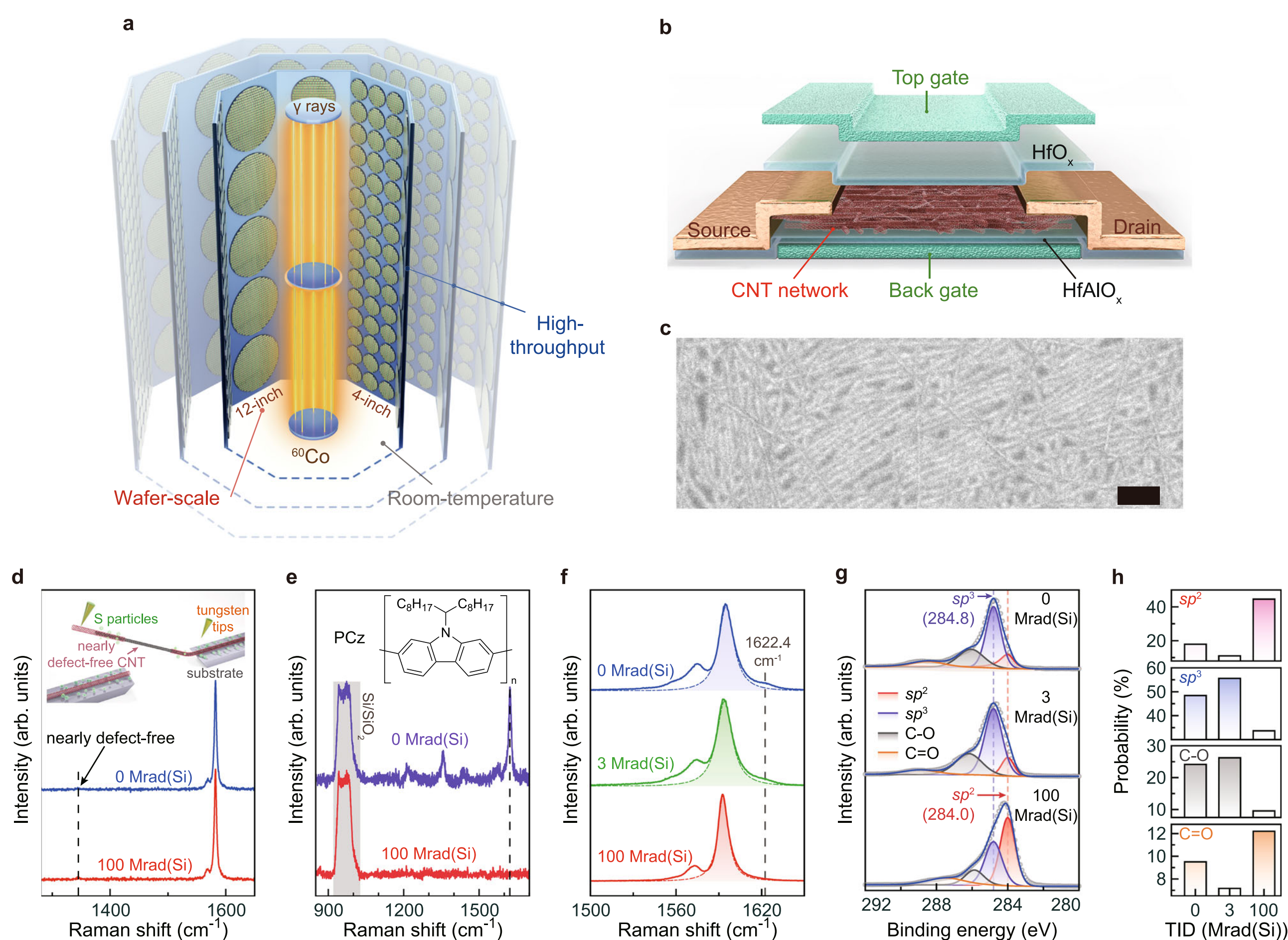


**Fig. 1 | A foundry-compatible strategy for enhancing the performance of carbon nanotube field-effect transistors (CNTFETs) through γ-ray irradition.** **a** Schematic diagram of γ-ray irradiation on wafer-scale CNTFETs. This room-temperature, high-throughput processing strategy meet the foundry requirements for efficiency, uniformity and cost-effectiveness. **b** Schematic diagram of the proposed quasi-gate-all-around (quasi-GAA) CNTFET, where the nanometer-thick CNT channel is modulated by two vertically connected gates. **c** Scanning electron microscopy (SEM) image of the deposited CNT network film. Scale bar: 100 nm. **d** Raman spectra of a single ultra-clean CNT before (0 Mrad(Si)) and after (100 Mrad(Si)) irradiation. The D peak remains negligible even after a total ionizing dose (TID) of 100 Mrad(Si), confirming the radiation tolerance of CNTs. The inset illustrates the process for obtaining an ultraclean CNT. **e** Raman spectra of conjugated PCz (poly[9-(1-octylonoyl)−9H-carbazole- 2,7-diyl]) molecules before (0 Mrad(Si)) and after (100 Mrad(Si)) irradiation. The inset displays the structural formula of PCz, with a characteristic wavenumber at 1622.4 cm$^{-1}$. **f** Raman spectra of CNT network films irradiated at 0 Mrad(Si), 3 Mrad(Si), and 100 Mrad(Si), respectively. The typical peak of PCz is indicated by a dashed line. **g** X-ray photoelectron spectroscopy (XPS) spectra of CNT network films irradiated at 0 Mrad(Si), 3 Mrad(Si), and 100 Mrad(Si), respectively. The peak positions for *sp*$^2$ and *sp*$^3$ are marked with dashed lines. **h** Area ratio of *sp*$^2$, *sp*$^3$, C-O, and C = O of CNT network films irradiated at 0 Mrad(Si), 3 Mrad(Si), and 100 Mrad(Si), respectively.

## Results

### γ-ray irradiation on carbon nanotubes

To validate our hypothesis, γ-ray irradiation was initially performed on a single ultra-clean CNT segment (1-2 walls) that was detached from a multi-walled structure[29,30]. A custom-built transfer stage with two tungsten tips was used to precisely position the CNT onto a $Si/SiO_2$ substrate (as shown in the inset of Fig. 1d, Supplementary Note. 4 and Supplementary Fig. 3). The Raman spectrum of the CNT segment exhibited an almost undetectable disordered signal at the D peak, confirming its pristine structure. The γ-ray irradiation was conducted at a dose rate of 300 rad(Si) $s^{-1}$ at room temperature, a condition that was consistently maintained throughout all subsequent experiments (Supplementary Note. 5). As illustrated in Fig. 1d, the D peak remained negligible even after a total ionizing dose (TID) of 100 Mrad(Si) (equivalent to 92.6 hours, with 1 rad ≈ 0.01 J $kg^{-1}$), clearly demonstrating the CNT's immunity to γ-ray irradiation (Supplementary Note. 6).

The polymer-sorted CNT film was further subjected to irradiation and subsequently analyzed using Raman spectroscopy and X-ray photoelectron spectroscopy (XPS). S-CNTs were separated using conjugated PCz (poly[9-(1-octylonoyl)−9H-carbazole- 2,7-diyl]) molecules[5,31–33] (as shown in the inset of Fig. 1e) and were then uniformly deposited onto a 4-inch $Si/SiO_2$ substrate (Supplementary Note. 7). Results from scanning electron microscopy (SEM) (Fig. 1c, Supplementary Fig. 4, and Supplementary Note. 8) and atomic force microscopy (AFM) (Supplementary Fig. 5) collectively confirm the high density and uniformity of the networked films.

As demonstrated in Fig. 1f, the Raman peak at 1622.4 $cm^{-1}$ exhibited a significant decrease following irradiation at a TID of 100 Mrad(Si) (Supplementary Note. 9). A detailed analysis indicated that this decline is likely due to the decomposition of the PCz polymer[21] (Fig. 1e). Furthermore, the D/G intensity ratio was employed to quantify the level of disorder in the CNT films. The results show that the D/G ratio initially increased up to 3 Mrad(Si) before gradually decreasing, which correlated with improved material performance at 100 Mrad(Si). A similar trend was observed in aligned CNT films, where organic materials such as PCz and 2-butene-1,4-diol were also utilized for sorting and alignment (Supplementary Note. 10 and Supplementary Fig. 6). We hypothesize that the changes in the D/G ratio are connected to the breaking and reformation of chemical bonds within the organic materials, while the CNTs themselves remain relatively stable during irradiation (Fig. 1d).

To elucidate this, XPS spectra were obtained for CNT films irradiated at 0 Mrad(Si), 3 Mrad(Si), and 100 Mrad(Si), covering an energy range of 280− 292 eV (Fig. 1g and Supplementary Note. 11). As TID increased to 3 Mrad(Si), the proportion of chemical bonds with higher bond dissociation energies (CB-HBDEs), such as $sp^2$ and C = O, showed a slight decrease, while the proportion of bonds with lower bond dissociation energies (CB-LBDEs), such as $sp^3$ and C-O, increased slightly (Fig. 1h). This change may be attributed to the decomposition of certain bonds within the organic materials, such as those between single and double bonds (e.g., benzene rings). In contrast, at a TID of 100 Mrad(Si), the proportion of CB-HBDEs notably increased, while the proportion of CB-LBDEs significantly decreased. This trend corresponds well with the changes observed in the D/G ratio from the Raman results (Supplementary Fig. 7 and Supplementary Note 12), indicating that high-dose γ-ray irradiation preferentially decomposes CB-LBDEs, leading to the formation of CB-HBDEs as part of a structural reorganization process (Supplementary Note 13 and Supplementary Fig. 8).

To assess the electrical performance of s-CNT films after γ-ray irradiation, top-gate (TG) CNTFETs were fabricated using both the original (0 Mrad(Si)) and irradiated (100 Mrad(Si)) films, following a similar methodology (Supplementary Fig. 9). To eliminate the impact of trapped charges induced by irradiation in the $Si/SiO_2$ substrate, a wet transfer process utilizing a sacrificial layer of polymethyl methacrylate (PMMA) was implemented to move the CNT films onto a new substrate (Supplementary Fig. 10). The results shown in supplementary Fig. 9 indicate a substantial reduction of 22.5% (332.9 mV $dec^{-1}$) in SS, along with a slight decrease of 31.1% in $I_{off}$ ($V_{ds}$ = 2.0 V). It is worth noting that interface gap states were reintroduced during the device fabrication due to the use of organic materials, such as PMMA and photoresist. These findings preliminarily suggest that γ-ray irradiation can enhance device performance.

### High-performance carbon nanotube transistors

A more suitable approach for industrialization would involve γ-ray post-treatment of the fabricated devices, rather than the CNT films themselves, which would help prevent the reintroduction of gap states during device processing. As shown in Fig. 1b, a quasi-gate-all-around (quasi-GAA) CNTFET is constructed on a 4-inch $Si/SiO_2$ substrate using standard photolithography and lift-off techniques (refer to the photograph in Fig. 2a and the fabrication processes detailed in supplementary Fig. 11). The term – quasi-GAA – refers to a nanometer-thick CNT channel that is controlled by two vertically connected gates. This design improves device reliability and gate efficiency compared to a single-gate configuration, resulting in increased $I_{on}$ and reduced SS. Unlike advanced GAA structures, the quasi-GAA configuration provides similar control effectiveness for devices with micro-scale channel lengths ($L_{ch}$), while offering a less complex fabrication process. Moreover, while established P-type doping technologies are available for CNTFETs[5,14,15,31,33–36], the development of N-type devices continues to pose significant challenges[20,32,37–40]. For example, low-work-function metals can create ohmic N-channel contacts, but their instability in air limits their use in irradiated environments. In this study, electrostatic doping through dielectric layers was employed, allowing for the tunneling injection of electrons from a palladium (Pd) electrode into the CNT channel (Supplementary Note. 14 and Supplementary Fig. 12). The channel length and width of the fabricated CNTFETs are 4 μm and 28 μm, respectively. Ti/Pd/Au (0.5/20/20 nm) stacks were utilized as the source/drain electrodes. The $HfO_x/HfAlO_x$ layers, which were deposited using atomic layer deposition (ALD) with a target thickness of 10 nm, served as both the dielectric and doping layers (Supplementary Notes. 15, 16). Cross-sectional transmission electron microscopy (TEM) imaging paired with the energy-dispersive X-ray spectroscopy (EDS) mapping, conducted both before and after irradiation, collectively confirms the radiation robustness of the fabricated CNTFETs (Fig. 2b–d, Supplementary Fig. 13 and Supplementary Notes. 17, 18).

The fabricated CNTFETs were characterized at room temperature and under ambient conditions. The typical transfer curves demonstrated a strong current density at $V_{gs}$ = 2 V, confirming that electrostatic doping successfully converted the initial CNTs to N-type polarity (Fig. 2e). The output characteristics revealed promising current control and saturation (Fig. 2f). The linear relationship of $I_{ds}$-$V_{ds}$ at low bias indicated that tunneling behaviors were not constrained by the sharp Schottky barrier in the contact region. This device achieved an impressive $I_{on}$ of 9.82 μA $\mu m^{-1}$ at a relatively low operating voltage ($V_{dd}$) of 2 V ($V_{gs} = V_{ds} = V_{dd}$, Supplementary Note 19), significantly surpassing the values reported in the literature (which range from approximately 0.01-1 μA $\mu m^{-1}$)[20,32–34,39,41–43]. Remarkably, the device achieved low SS values of 102.0 mV $dec^{-1}$ at low bias (50 mV) and 173.7 mV $dec^{-1}$ at saturated bias (2 V), despite having a relatively thick gate oxide stack (~10 nm). These performance enhancements exceeded those of N-type network-based CNTFETs. For comparison, the $I_{on}$ versus SS values from the literature and those obtained in this study, focusing on micrometer-scale $L_{ch}$, are plotted in Fig. 2g. This comparison highlights that our devices provide superior $I_{on}$ while maintaining low SS, primarily due to the excellent gate efficiency of our quasi-GAA architecture (Fig. 2g, Supplementary Fig. 14, and

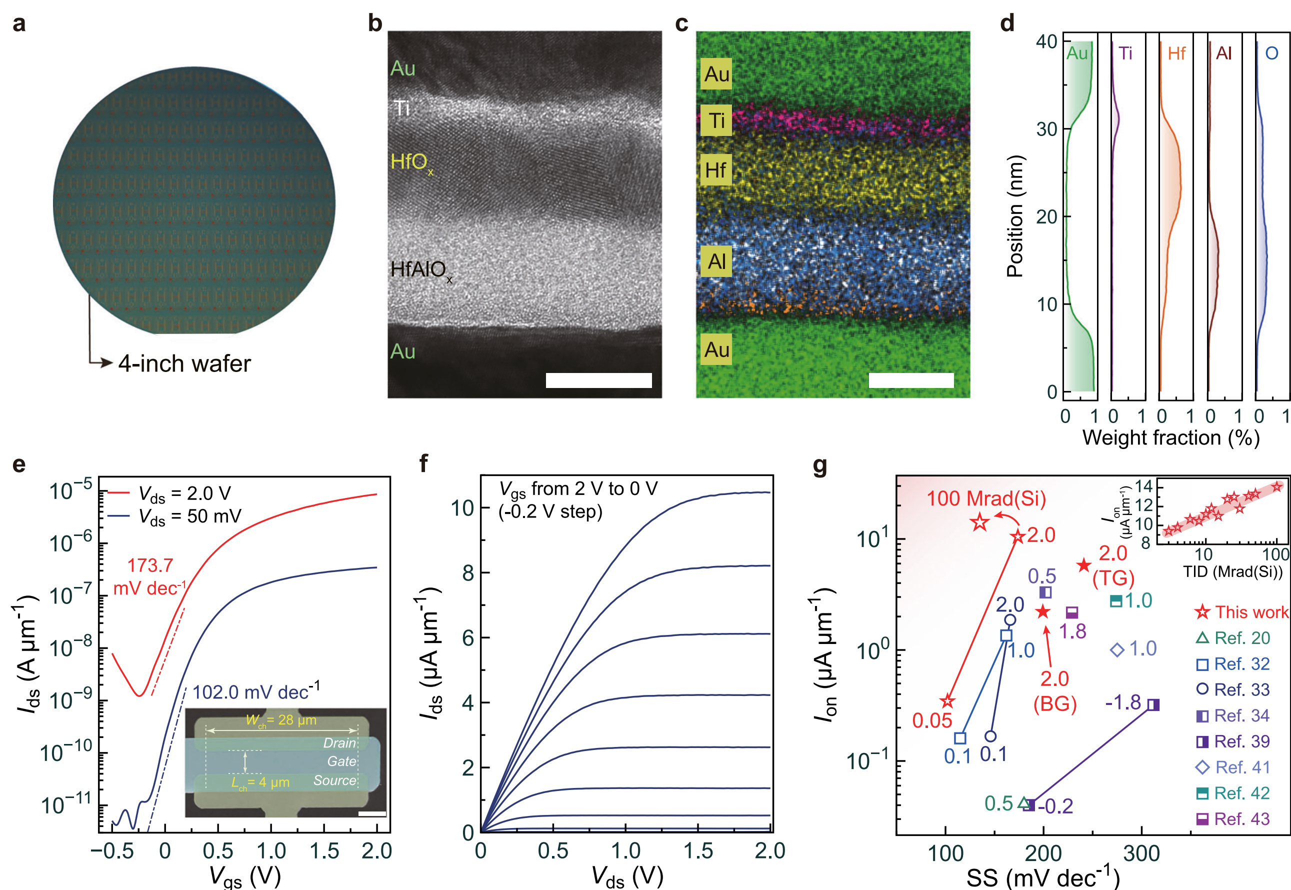


**Fig. 2 | High-performance quasi-GAA CNTFETs. a** Photograph of the as-fabricated CNTFETs on a 4-inch Si/$SiO_2$ substrate. **b** Cross-sectional high-resolution transmission electron microscope (TEM) image of the as-fabricated CNTFET. Scale bar: 10 nm. **c** Cross-sectional energy dispersive X-ray spectroscopy (EDS) mapping of the as-fabricated CNTFET, see Supplementary Note. 18 for more details. Scale bar: 10 nm. **d** EDS line analysis of the following elements: Gold (Au), Titanium (Ti), Hafnium (Hf), Aluminum (Al), and Oxygen (O). **e** Typical transfer curves of the CNTFET at drain-to-source voltage ($V_{ds}$) of 2 V and 50 mV, respectively. The subthreshold swing (SS) of the device is 102.0 mV dec$^{-1}$ at low bias (50 mV) and 173.7 mV dec$^{-1}$ at saturated bias (2 V). Inset: False-color SEM image of the representative CNTFET, with a channel length ($L_{ch}$) and width of 4 μm and 28 μm, respectively. Scale bar: 5 μm. **f** Typical output curves of the CNTFET with gate-to-source voltage ($V_{gs}$) varying from 2 V to 0 V in step of − 0.2 V. **g** Benchmarking of on-state current ($I_{on}$) versus SS of our results with reported N-type networked CNTFETs with micrometer $L_{ch}$. $V_{ds}$ is labeled in the figure. Inset plots the experimental results of $I_{on}$ versus TID.

Supplementary Note. 20) and the optimized fabrication processes that ensure a relatively clean interface.

### γ-ray irradiation on carbon nanotube transistors

Subsequently, γ-ray irradiation was performed on the CNTFETs under unbiased conditions. After exposure to a specific dose, controlled by the irradiation time, tests were conducted to evaluate any changes in their electrical performance. A total of 25 devices were selected for statistical analysis. The transfer curves of these devices prior to irradiation exhibited minimal performance variability, indicating the suitability of the quasi-GAA devices for large-scale foundry production (Fig. 3a). Typically, irradiation-induced trapped charges can impair the performance of CNTFETs, particularly by causing shifts in $V_{th}$. However, for the proposed quasi-GAA architecture, trapped charges from the substrate and the surrounding environment were effectively shielded by the bottom and top gate electrodes, respectively. As a result, even after irradiation doses of up to 100 Mrad(Si), the fluctuation in $V_{th}$ remained negligible (within 10% of $V_{dd}$), underscoring the robustness of the quasi-GAA architecture in radiation environments. In addition, the gate-to-source current ($I_{gs}$) remained at an ultralow level (~3 pA) throughout the entire irradiation process, indicating that the dielectric layers were not compromised by the γ rays (Supplementary Note 21, and Supplementary Figs. 15, 16). Figure 3b illustrates the transfer curves of a typical device after exposure to doses of 0 Mrad(Si), 3 Mrad(Si), and 100 Mrad(Si). At 3 Mrad(Si), some performance degradation was observed, characterized by a 2.4-fold increase in $I_{off}$ and a 28.5 mV dec$^{-1}$ rise in SS. However, surprisingly, after irradiation at 100 Mrad(Si), the device performance improved: $I_{on}$ increased by 54.9% to 14.33 μA μm$^{-1}$, $I_{off}$ decreased by more than an order of magnitude to 157.7 pA μm$^{-1}$, and SS reduced by 57.0 mV dec$^{-1}$ to 144.7 mV dec$^{-1}$.

These variations were further supported by statistical analysis. It was observed that the trends of $I_{on}$ and $I_{off}$ consistently displayed opposite behaviors, with their changes being markedly different. This suggests that the counterintuitive behavior of the devices was primarily influenced by channel properties rather than contact resistance (Supplementary Notes. 22, 23 and Supplementary Figs. 17, 18). This conclusion is reinforced by the correlation between the materials' D/G ratio and the devices' performance. Specifically, an increasing proportion of CB-LBDEs, such as $sp^3$ and C-O, was consistently associated with a higher D/G ratio and deteriorating device performance, evidenced by decreased $I_{on}$, increased $I_{off}$, and higher SS values. In contrast, an increasing presence of CB-HBDEs, such as $sp^2$ and C = O, correlated with a lower D/G ratio and enhanced device performance (Supplementary Note 24 and Supplementary Fig. 17). We attribute this behavior to gap states within the bandgap of CNTs (Fig. 3c, d). These

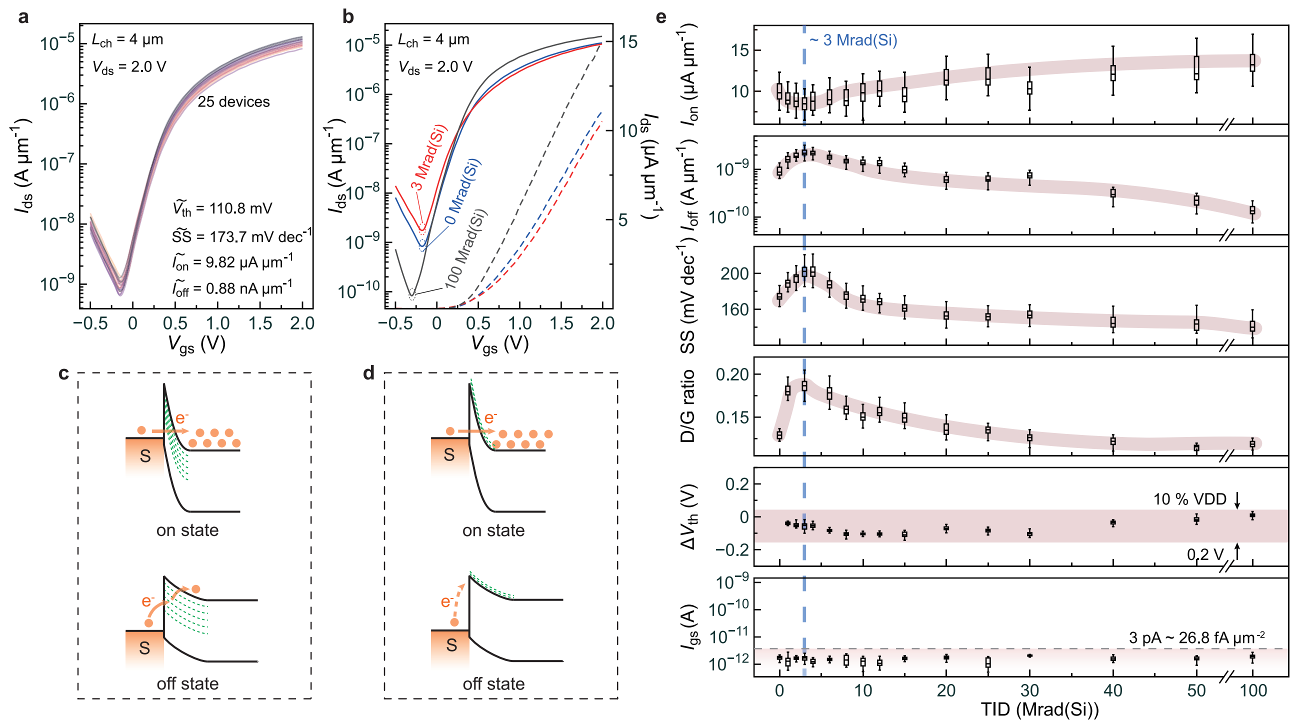

**Fig. 3 | γ-ray irradiation effects on CNTFETs. a** Transfer curves of 25 devices used for subsequent irradiation tests. The inset displays the median values of typical electrical parameters. **b** Transfer curves of a typical CNTFET irradiated at 0 Mrad(Si), 3 Mrad(Si), and 100 Mrad(Si), respectively. Solid lines represent logarithmic coordinates, and dashed lines represent linear coordinates. **c** Band diagrams of the CNTFETs irradiated at 3 Mrad(Si) (worst condition). **d** Band diagrams of the CNTFETs irradiated at 100 Mrad(Si) (best condition). **e** Performance variation of CNTFETs and CNT films within the TID range of 0 to 100 Mrad(Si). As the TID increases, device performance initially deteriorates and then gradually improves, with an inflection point at 3 Mrad(Si). Within 100 Mrad(Si), the threshold voltage ($V_{th}$) and gate-to-source current ($I_{gs}$) experience negligible changes. The box plots show the median (center line), interquartile range (box boundaries), and minimum/maximum values (whiskers).

gap states, typically resulting from chemical doping interactions involving adjacent CB-LBDEs, can facilitate the electron tunneling process from the Pd source electrode to the CNT channel, leading to increased $I_{off}$. In addition, the density of interface states can also enhance SS values (Supplementary Note 25). However, γ-ray irradiation tends to convert these CB-LBDEs into CB-HBDEs, which are often linked to the formation of delocalized π electrons, introducing electron doping in the conduction band of s-CNTs or deep within the bandgap. As the shallow gap states are reduced, both $I_{off}$ and SS can significantly decrease, while the improvement in $I_{on}$ is less pronounced due to the relatively low content of organics, achieved through optimized material selection and device fabrication processes (Fig. 3e, Supplementary Fig. 18, Supplementary Note. 19 and Supplementary Note 26).

### Reliable γ-ray irradiation strategy

The effectiveness of γ-ray irradiation in enhancing electrical performance was further confirmed through statistical measurements. As shown in Fig. 4a, b, a relatively low device-to-device variation was noted before and after irradiation across 100 devices fabricated on a $Si/SiO_2$ substrate, indicating the viability of the proposed quasi-GAA architecture for large-scale manufacturing and γ-ray treatment. Furthermore, $V_{th}$ of the irradiated devices remained nearly unchanged (approximately 1.4% of $V_{dd}$), while SS decreased by 41 mV $dec^{-1}$ to 134.9 mV $dec^{-1}$, and $I_{off}$ was reduced by an order of magnitude to 112.2 pA $\mu m^{-1}$ (Supplementary Fig. 19). These improvements align with the previously mentioned results, underscoring that γ-ray irradiation serves as a robust and effective method for enhancing the performance of CNTFETs. Notably, γ-ray irradiation on non-silicon substrates (photosensitive polyimide, PSPI) and CNTFETs with 600 nm channel lengths – including both network-based and array-based architectures – can also achieve similar enhancements, further demonstrating the reliability of this technique (Fig. 4c, d, Supplementary Notes 27–30, and Supplementary Figs. 20–23). Importantly, since irradiation causes permanent damage to polymers, the performance improvements do not degrade over time (Supplementary Note 31 and Supplementary Fig. 24).

## Discussion

Under ultra-small bias conditions, CNTFETs are often characterized by low $I_{off}$ and high on/off ratios[5,20,26,31,32,34,44–47]. However, assessing these parameters at operational voltages ($V_{dd}$) is more pertinent for practical circuit applications[48], such as complementary metal oxide-semiconductor (CMOS) technology and ring oscillators (Supplementary Fig. 25). Although quasi-GAA CNTFETs have shown an order of magnitude improvement in both $I_{off}$ and on/off ratio compared to as-fabricated TG devices, their performance remains moderate compared to other reported CNTFETs with micrometer-scale channel lengths[14,15,32,33,39,40,43,49]. Further enhancements are hindered by the presence of organic-induced gap states. With the proposed γ-ray treatment, however, the performance of quasi-GAA CNTFETs in terms of $I_{off}$ and on/off ratio is improved by another order of magnitude, achieving the highest levels for these metrics (Fig. 4e). Typically, a dose of 100 Mrad(Si) can reduce $I_{off}$ to the low-power target[15] of 100 pA $\mu m^{-1}$ due to the reduction in gap states.

Another notable finding of this study is the exceptional radiation tolerance demonstrated by our quasi-GAA CNTFETs, capable of withstanding approximately 100 Mrad(Si). This property shows considerable potential for deployment in high-radiation scenarios like deep-space missions, nuclear reactor operations, and radiation therapy procedures[50]. Traditional silicon-based transistors, even those designed with radiation-hardened processes, generally fail to endure

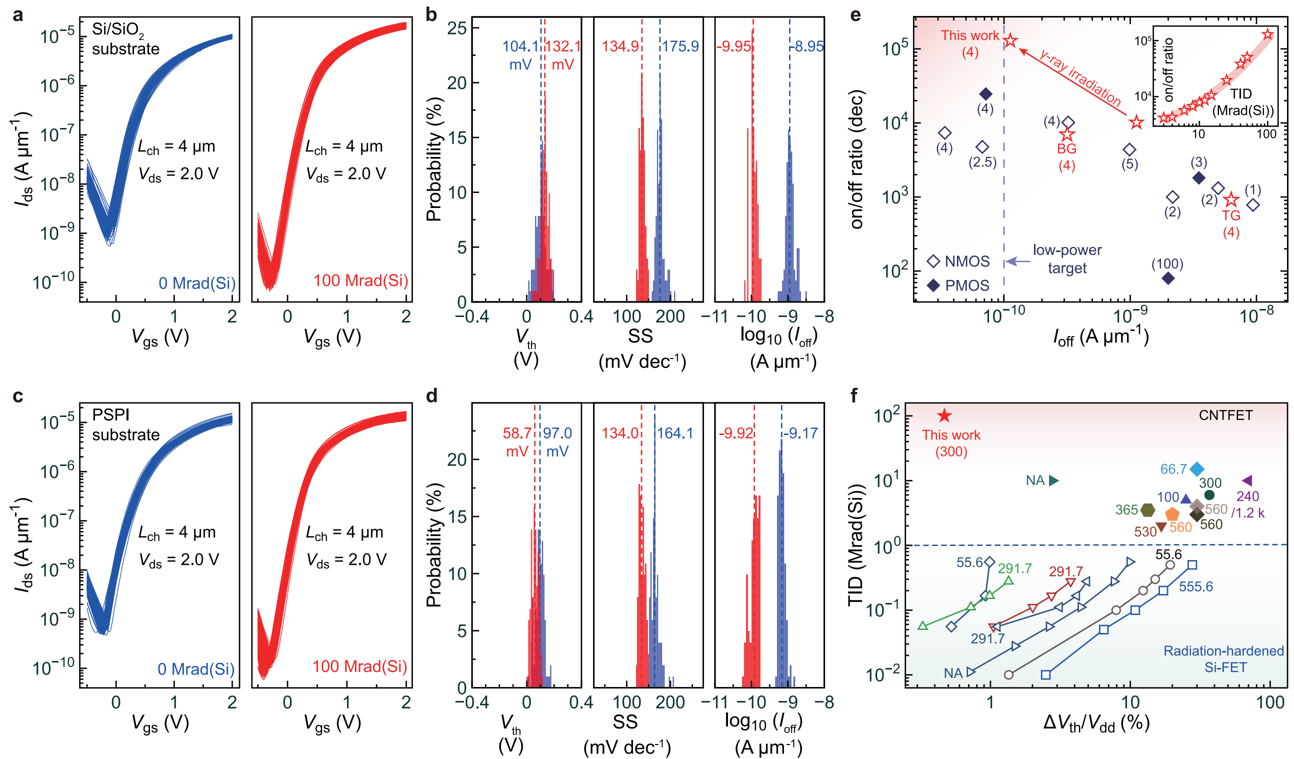


**Fig. 4 | Reliable γ-ray irradiation strategy. a** Transfer curves of 100 devices, fabricated on a Si/$SiO_2$ substrate, before (0 Mrad(Si)) and after (100 Mrad(Si)) irradiation. **b** Statistical analysis of the $V_{th}$, SS, and $I_{off}$ of devices in (**a**). **c** Transfer curves of 100 devices, fabricated on a Si/$SiO_2$/PSPI substrate, before (0 Mrad(Si)) and after (100 Mrad(Si)) irradiation. **d** Statistical analysis of the $V_{th}$, SS, and $I_{off}$ of devices in (**c**). **e** Benchmarking of the on/off ratio versus $I_{off}$ of our results at $V_{ds}$ = 2 V with reported CNTFETs with micrometer-scale $L_{ch}$. Hollow and solid patterns represent N-type[32,33,39,40,43] and P-type[14,33,49] CNTFETs, respectively. $L_{ch}$ (μm) is labeled in the figure. The low-power target for transistors at 100 pA μm$^{-1}$ is indicated by a dashed line. The inset plots the experimental results of the on/off ratio and TID. **f** Benchmarking of TID tolerance versus $\Delta V_{th}/V_{dd}$ of our results with reported radiation-hardened transistors. The hollow pattern represents silicon transistors[51–55], while the solid pattern represents CNTFETs[26–28,56–60]. Dose rate (rad(Si) s$^{-1}$) is labeled in the figure, and NA indicates the dose rate is not available in those references.

TID levels of 1 Mrad(Si)[51–55]. In contrast, CNT channels typically exhibit reported TID tolerances ranging from 1 to 10 Mrad(Si)[26–28,56–60], thanks to their lower hit probabilities and higher BDEs. The proposed quasi-GAA architecture, with its nearly ideal electrostatic shielding, achieves a TID tolerance of 100 Mrad(Si) without compromising the $V_{th}$ by more than 10% of the supply voltage ($V_{dd}$). This represents a two-order-of-magnitude improvement over silicon devices and a one-order-of-magnitude enhancement compared to previously reported CNTFETs (Fig. 4f). Despite these advancements, further research is necessary before integrating CNTFETs into practical irradiation environments, particularly to understand their behavior under operational conditions.

We have developed a foundry-friendly method to enhance the performance of CNTFETs through γ-ray irradiation. This room-temperature processing technique is compatible with wafers of various sizes, ranging from 4 to 12 inches, facilitating large-scale production of CNTFETs while meeting foundry requirements for high efficiency, uniformity, and cost-effectiveness. Characterization using Raman spectroscopy and X-ray photoelectron spectroscopy revealed that high-energy, low-beam γ rays do not damage the pristine structure of CNTs but instead induce a transformation in the chemical bonds of the organics surrounding them, shifting from low-energy to high-energy bonds. This transformation was further validated at the device level through the fabrication of quasi-GAA CNTFETs. The comprehensive performance metrics, including an $I_{on}$ of 9.82 μA μm$^{-1}$ and SS values of 102.0 mV dec$^{-1}$ at a 50 mV bias and 173.7 mV dec$^{-1}$ at a 2 V saturated bias, represent some of the best results reported in the literature for N-type networked CNTFETs with micrometer-scale channel lengths ($L_{ch}$). Statistical analysis of γ-ray irradiation across 100 devices indicated that the SS decreased by 41 mV dec$^{-1}$, reaching 134.9 mV dec$^{-1}$. The $I_{off}$ was reduced by an order of magnitude to 112.2 pA μm$^{-1}$, approaching the low-power transistor target of 100 pA μm$^{-1}$. The on/off ratio (~$10^5$) achieved the highest level recorded among networked CNTFETs under saturated bias conditions (Supplementary Note 32). The performance enhancements resulting from γ-ray irradiation can be attributed to the reduction of shallow gap states due to an increase in the content of CB-HBDEs. The proposed quasi-GAA architecture exhibits a $V_{th}$ shift of less than 10% of $V_{dd}$ during a TID of 100 Mrad(Si), outperforming traditional silicon-based devices by at least two orders of magnitude and advanced radiation-hardened CNTFETs by one order of magnitude. In summary, our work presents an optimal, foundry-friendly strategy for enhancing the performance of CNTFETs through γ-ray treatment, broadening their application prospects in radiation-heavy environments.

## Methods

### Power estimation of different processing methods

This section will separately estimate the power (energy per unit time) of three processing methods on a single CNT segment: γ-ray irradiation, high-temperature annealing, and e-beam irradiation. Given that the diameter of a focused e-beam is approximately 10 nm ($D_{e\text{-beam}}$), we will consider a CNT segment with a length ($L$) of 10 nm and a diameter ($d$) of 1 nm for estimation. This simplification will not affect the qualitative conclusions.

In γ-ray irradiation, the dose rate, defined as the energy acting on unit mass per unit time, is commonly used to quantify the intensity of

γ-rays. The mass ($m_{CNT}$) of the CNT segment can be estimated by calculating the number of carbon atoms ($N_{carbon}$) using the following relationship.

$$N_{carbon} = \frac{L}{l_{CB}} \times \frac{\pi d}{l_{CB}} = \frac{L\pi d}{l_{CB}^2} \quad (1)$$

where $l_{CB}$ is the bond length of CNTs ($l_{CB}$ = 0.142 nm). Thus, the mass of the CNT segment is:

$$m_{CNT} = N_{carbon} \times m_0 \quad (2)$$

here, $m_0$ is the mass of a single carbon atom ($m_0 = 1.993 \times 10^{-26}$kg).

In our experiment, a dose rate of 300 rad(Si) s$^{-1}$ is adopted. It should be emphasized that this value is calibrated using silicon materials. For CNTs, the corresponding conversion relationship is:

$$D_{CNT} = D_{Si} \times \left( \frac{(\mu/\rho)_{CNT} \cdot \rho_{CNT}}{(\mu/\rho)_{Si} \cdot \rho_{Si}} \right) \quad (3)$$

where $D_{CNT(Si)}$ is the dose rate calibrated by the CNT (silicon). The mass attenuation coefficient (MAC) of CNTs and silicon are estimated to be 0.0569 cm$^2$g$^{-1}$ and 0.05688 cm$^2$g$^{-1}$, respectively[61]. The densities of CNTs and silicon are 1.6 g cm$^{-3}$ and 2.33 g cm$^{-3}$, respectively. Consequently, the dose rate quantified by CNTs ($D_{CNT}$) is 206.1 rad(CNT) s$^{-1}$ or 2.061 J kg$^{-1}$ s$^{-1}$.

Finally, the power acting on the single CNT segment from γ-rays ($P_{\gamma-ray}$) is estimated to be $6.4 \times 10^{-21}$ W using the following formular:

$$P_{\gamma-ray} = m_{CNT} \times D_{CNT} \quad (4)$$

In high-temperature annealing, the annealing temperature is typically set to 600 °C ($T$ = 873.15 K), and the power of thermal radiation can be described using the Stefan-Boltzmann law (Supplementary Note 33). According to this law, the thermal radiation power ($P_{thermal}$) is given by:

$$P_{thermal} = \varepsilon \sigma T^4 A \quad (5)$$

where $\varepsilon$ is the emissivity of carbons, which is approximately 0.81[62], $\sigma$ is the Stefan-Boltzmann constant, $A$ is the surface area of the CNT segment, calculated as $A = \pi dL$.

By substituting the respective values, the power for high-temperature annealing is estimated to be $8.39 \times 10^{-13}$ W.

In e-beam irradiation, assuming the e-beam energy ($E_{e-beam}$) is 10 keV and the specimen current ($I_{e-beam}$) is 100 pA, the number of electrons in the e-beam per second can be calculated using the following formular:

$$N_e = \frac{I_{e-beam}}{e} \quad (6)$$

where $e$ is the elementary charge. The power acting on the single CNT segment from the e-beam can be calculated using:

$$P_e = \eta N_e \times E_{e-beam} \quad (7)$$

here, $\eta$ is the action possibility, which has a minimum value of 0.128 determined by the area ratio of the CNT segment ($\frac{Ld}{\pi (D_{e-beam}/2)^2}$).

Thus, the minimum power for e-beam irradiation is estimated to be $1.27 \times 10^{-7}$ W.

### Estimation of wafer processing throughput

As depicted in Supplementary Fig. 2, the γ-ray source (height: $L$) is positioned at the center of the irradiation environment. For a ring with a specific radius $R_0$, the number of wafers (diameter: $D$) that can be treated is given by:

$$N_0 = \lfloor L/D \rfloor \times \lfloor (2\pi R_0)/D \rfloor \quad (8)$$

where $\lfloor x \rfloor$ donates rounding down the calculated value $x$.

Assuming that wafers are arranged in rings with radii ranging from $r$ to $R$, and the spacing between adjacent rings is $\Delta r$, the total number of wafers ($N$) that can be processed simultaneously in this irradiation setup is:

$$N = \sum_{R_0 = r}^{R_0 = R} N_0 \quad (9)$$

For objectivity, let's consider $r = 0.5$ m, $R = 2.0$ m, $\Delta r = 0.1$ m, and $l = 1.0$ m. Then, for 12-inch wafers ($D$ = 300 mm), $N = 1,230$, while for 4-inch wafers ($D$ = 100 mm), $N = 12,480$. In our experiment, an irradiation dose of 100 Mrad(Si) required 92.6 hours. As an estimate, this setup could process ~ 8610 12-inch wafers or ~ 87,360 4-inch wafers.

### Growth and manipulation of ultralong carbon nanotubes

Ultralong CNTs were grown on hollow Si/$Si_3N_4$ substrates using the chemical vapor deposition (CVD) method. Initially, a 0.2 nm iron catalyst was deposited on a Si/$SiO_2$ substrate through e-beam evaporation. Subsequently, a super-aligned cross-stacked CNT film was placed on the surface of the substrate[63]. This film facilitated the detachment of the grown CNTs from the Si/$SiO_2$ substrate. Under the influence of an airflow containing $C_2H_4$ (1.0 sccm), Ar (452 sccm), and $H_2$ (216 sccm), the elongating CNTs were directed to drift and eventually settled on the pre-positioned hollow Si/$Si_3N_4$ substrate.

Ultralong suspended CNTs were then manipulated using two tungsten tips prepared via electrochemical etching. Initially, supported by a hollow Si/$Si_3N_4$ substrate, the CNTs were positioned above sulfur (S) vapor, allowing S particles to condense on their surface. This step was crucial for visualizing the nanoscale CNTs under an optical microscope. With the help of manipulators, the tungsten tips were used to touch and slide the end of a single CNT, causing it to detach from the substrate and adhere to the tip surface through van der Waals forces. Subsequently, a designed substrate was positioned beneath the tips, and the tips were maneuvered to place the CNT onto the specified substrate. Finally, the substrate was heated on a 170 °C hot plate for 2 min to remove the S particles from the CNT surface.

### Preparation of carbon nanotube films

CNTs synthesized via arc-discharge using Ni/Y catalysts were sourced commercially from Carbon Solutions Inc. For selective extraction of semiconducting CNTs, the conjugated polymer PCz – synthesized through Suzuki polycondensation – served as a sorting agent. In this purification protocol, 100 mg of raw CNTs and 200 mg of PCz were dispersed in 100 mL of toluene. The suspension underwent 30 min ultrasonication with a top-tip dispergator (Sonics VC500), followed by centrifugation at 30,000 × $g$ for 2 h (Allegra X-64R centrifuge) to isolate a semiconducting-enriched supernatant. Prior to film fabrication, substrates were cleaned in sequential solvent baths (toluene, acetone, and isopropanol). These substrates were then submerged in the purified CNT dispersion for 24 h, dried under a nitrogen stream, and annealed at 120 °C for 30 min on a hotplate.

Well-aligned CNT arrays were obtained using a dimension-limited self-alignment (DLSA) procedure. In detail, the high-purity semiconducting CNT solution was re-dispersed in 1,1,2-trichloroethane. The substrate was then vertically inserted into the CNT solution, followed

by dropping a $C_4H_8O_2$ solution. As the substrate was slowly extracted from the solutions, CNTs became confined to the 2D interface between the $C_4H_8O_2$ and 1,1,2-trichloroethane solutions. Due to the strong affinity of $C_4H_8O_2$ for $SiO_2$, the CNTs assembled onto the substrate surface almost in parallel.

### Transfer of carbon nanotube films

PMMA was utilized as a sacrificial layer to transfer the CNT film to an unirradiated Si/$SiO_2$ substrate (Supplementary Fig. 10). Initially, a layer of PMMA was spin-coated onto the irradiated substrate at 3000 r min$^{-1}$ for 1 min. The substrate was then immersed in electronic-grade ammonia water at room temperature. After the PMMA-coated CNT film detached from the substrate, it was rinsed twice with ultra-pure water. The PMMA film was subsequently lifted off using a clean, unirradiated substrate. Once the residual water evaporated naturally, the sample was baked on a hotplate at 90 °C for 5 min. Finally, the CNT film was transferred following sequential treatments with acetone, N-methyl-2-pyrrolidone (NMP), and ultra-pure water.

### Characterizations of carbon nanotubes

Raman spectroscopy was conducted on the HORIBA LabRAM HR Evolution spectrometer with a laser wavelength of 532 nm and an 1800 mm$^{-1}$ grating. The spectral data were calibrated using the silicon characteristic peak at 520.7 cm$^{-1}$ on an undoped silicon specimen. Prior to Raman measurements on an individual CNT, its position was roughly determined using S vapor tagging. Subsequently, Raman line scanning was employed to collect spectroscopic data, with the data featuring the strongest signal being considered as the Raman spectrum of the CNT. For Raman analysis of PCz, PCz was dissolved in toluene and then spin-coated onto a Si/$SiO_2$ substrate at 3000 r min$^{-1}$ for 1 min.

XPS data were acquired using a Thermo Fisher Scientific ESCALAB Xi+ spectrometer with a best energy resolution of less than 0.43 eV. All spectral data were calibrated using the C1s peak at 284.8 eV. High-resolution TEM images were observed using an FEI Talos F200S G2 equipment. SEM was conducted using a Zeiss GENMINI SEM 500 setup. AFM was performed with a Bruker Dimension FastScan operating in tapping mode. Optica images were captured using a Nikon MM-400/L.

### Device fabrication and measurements

Standard techniques were employed to fabricate all CNTFETs (Supplementary Fig. 11). For instance, the electrodes were fabricated using photolithography and lift-off processes. The vacuum level during e-beam evaporation was typically better than $10^{-4}$ Pa. The gate insulating layers were grown using the ALD at a temperature of 90 °C, with a specified thickness of 10 nm. To enhance nucleation sites on the CNT surfaces and thereby improve material growth quality, water vapor was introduced as the initial precursor.

For dual-gate devices, Ti/Au (1/40 nm) electrodes were initially patterned and evaporated onto a precleaned substrate. Subsequently, the $HfAlO_x$ bottom gate dielectric was grown using the ALD technique. This was followed by the deposition of the CNT network film. It should be emphasized that 10 nm of Y was deposited and subsequently removed using dilute hydrochloric acid to further clean the CNT films[64]. Next, the CNT channel was defined through an oxygen plasma process, and the source/drain electrodes (Ti/Pd/Au ~ 0.5/20/20 nm) were patterned. Following this, the $HfO_x$ top gate dielectric was grown using the ALD technique as well. Finally, the top gate electrode, composed of Ti/Au (1/40 nm), was patterned and evaporated.

For the PSPI substrate shown in Fig. 4c, a layer of PSPI photoresist (~500 nm thick) was spun onto a Si/$SiO_2$ substrate and baked at 120 °C, 180 °C, 240 °C, and 300 °C for 30 min each to fully solidify the polymer. The fabrication processes for TG and BG devices were very similar to that of quasi-GAA devices. Notably, the TG device did not involve the preparation of the bottom-gate electrode and bottom-gate dielectric, while the BG devices did not require the preparation of the top-gate electrode. All electrical measurements were carried out at room temperature and atmospheric pressure, utilizing self-made programs based on the LabVIEW software.

The detailed extraction methods of $V_{th}$ could be found in ref. 65. In our work, $V_{th}$ was extracted from the gate voltage axis intercept of the $\sqrt{I_{ds}} \sim V_{gs}$ characteristics linearly extrapolated at its maximum first derivative point.

### Irradiation process

In this experiment, $^{60}$Co served as the irradiation source with a half-life of 5.27 years. Its decay produced non-radioactive $^{60}$Ni, accompanied by the emission of β particles and two types of γ rays with energies of 1.17 MeV and 1.33 MeV ($_{27}{}^{60}\mathrm{Co} \rightarrow {}_{28}{}^{60}\mathrm{Ni} + {}_{-1}{}^{0}\beta + {}_{0}{}^{0}\gamma$). A stainless-steel casing was employed to shield the β particles, thereby ensuring a stable emission of γ rays. The cobalt rod was typically housed in a water tank and was only retrieved for the experiment when necessary.

The TID was directly proportional to the irradiation duration. In our experiment, the dose rate, which is the proportionality constant, was maintained at 300 rad(Si) s$^{-1}$. To achieve a TID of 100 Mrad(Si), a total irradiation time of 92.6 h was required.

## Data availability

The authors declare that data generated in this study are provided in the paper and the Supplementary Information file. Further datasets are available from the corresponding author upon request.

## References


1. Khan, H. N., Hounshell, D. A. & Fuchs, E. R. Science and research policy at the end of Moore's law. *Nat. Electron.* **1**, 14–21 (2018).
2. Cao, W. et al. The future transistors. *Nature* **620**, 501–515 (2023).
3. Li, M.-Y., Su, S.-K., Wong, H.-S. P. & Li, L.-J. How 2D semiconductors could extend Moore's law. *Nature* **567**, 169–170 (2019).
4. Qiu, C. et al. Scaling carbon nanotube complementary transistors to 5-nm gate lengths. *Science* **355**, 271–276 (2017).
5. Liu, L. et al. Ma Z. Aligned, high-density semiconducting carbon nanotube arrays for high-performance electronics. *Science* **368**, 850–856 (2020).
6. Cheng, X., Pan, Z., Fan, C., Wu, Z., Ding, L. & Peng, L.M. Aligned carbon nanotube–based electronics on glass wafer. *Sci. Adv.* **10**, eadl1636 (2024).
7. Cao, Q., Tersoff, J., Farmer, D. B., Zhu, Y. & Han, S.-J. Carbon nanotube transistors scaled to a 40-nanometer footprint. *Science* **356**, 1369–1372 (2017).
8. Wang, J. et al. Growing highly pure semiconducting carbon nanotubes by electrotwisting the helicity. *Nat. Catal.* **1**, 326–331 (2018).
9. Zhang, S. et al. Arrays of horizontal carbon nanotubes of controlled chirality grown using designed catalysts. *Nature* **543**, 234–238 (2017).
10. Cao, Q. et al. End-bonded contacts for carbon nanotube transistors with low, size-independent resistance. *Science* **350**, 68–72 (2015).
11. Hills, G. et al. Modern microprocessor built from complementary carbon nanotube transistors. *Nature* **572**, 595–602 (2019).
12. Shulaker, M. M. et al. Three-dimensional integration of nanotechnologies for computing and data storage on a single chip. *Nature* **547**, 74–78 (2017).
13. Shulaker, M. M. et al. Carbon nanotube computer. *Nature* **501**, 526–530 (2013).
14. Si, J. et al. A carbon-nanotube-based tensor processing unit. *Nat. Electron.* **7**, 684–693 (2024).
15. Bishop, M. D. et al. Fabrication of carbon nanotube field-effect transistors in commercial silicon manufacturing facilities. *Nat. Electron.* **3**, 492–501 (2020).
16. Cao, Q. Carbon nanotube transistor technology for More-Moore scaling. *Nano Res.* **14**, 3051–3069 (2021).

17. Cheng C.-C. et al. Monolithic heterogeneous integration of BEOL power gating transistors of carbon nanotube networks with FEOL Si ring oscillator circuits. In *2019 IEEE International Electron Devices Meeting (IEDM)*) (2019).
18. Pitner G. et al. Building high performance transistors on carbon nanotube channel. In *2023 IEEE Symposium on VLSI Technology and Circuits (VLSI Technology and Circuits)* (2023).
19. Li, S. et al. High-performance and low parasitic capacitance CNT MOSFET: 1.2 mA/μm at V DS of 0.75 V by self-aligned doping in sub-20 nm spacer. In the *2023 International Electron Devices Meeting (IEDM)*(2023).
20. Zhang, Z. et al. Complementary carbon nanotube metal–oxide–semiconductor field-effect transistors with localized solid-state extension doping. *Nat. Electron.* **6**, 999–1008 (2023).
21. Han, J., Xu, X. & Zhang, Z. Removing conjugated polymers from aligned carbon nanotube arrays. *Small* **20**, e2309654 (2024).
22. Han, J., Xu, X. & Zhang, Z. Removal of conjugated polymer on carbon nanotube array by dry process. *Carbon* **223**, 119050 (2024).
23. Li, J. & Banhart, F. The engineering of hot carbon nanotubes with a focused electron beam. *Nano Lett.* **4**, 1143–1146 (2004).
24. Banhart, F., Li, J. X. & Krasheninnikov, A. V. Carbon nanotubes under electron irradiation: Stability of the tubes and their action as pipes for atom transport. *Phys. Rev. B* **71**, 241408 (2005).
25. Prinzie, J., Simanjuntak, F. M., Leroux, P. & Prodromakis, T. Low-power electronic technologies for harsh radiation environments. *Nat. Electron.* **4**, 243–253 (2021).
26. Zhu, M. et al. Radiation-hardened and repairable integrated circuits based on carbon nanotube transistors with ion gel gates. *Nat. Electron.* **3**, 622–629 (2020).
27. Kanhaiya, P. S. et al. Carbon nanotubes for radiation-tolerant electronics. *ACS Nano* **15**, 17310–17318 (2021).
28. Zhang, K. et al. Large-scale complementary carbon nanotube integrated circuits for harsh radiation environments. *Sci. Adv.* **11**, eadw0024 (2025).
29. Zhang, R. et al. Superlubricity in centimetres-long double-walled carbon nanotubes under ambient conditions. *Nat. Nanotechnol.* **8**, 912–916 (2013).
30. Zhang, K. et al. Electrical control of spatial resolution in mixed-dimensional heterostructured photodetectors. *Proc. Natl. Acad. Sci. USA* **116**, 6586–6593 (2019).
31. Zhong, D. et al. Gigahertz integrated circuits based on carbon nanotube films. *Nat. Electron.* **1**, 40–45 (2017).
32. Yang, Y., Ding, L., Han, J., Zhang, Z. & Peng, L. M. High-performance complementary transistors and medium-scale integrated circuits based on carbon nanotube thin films. *ACS Nano* **11**, 4124–4132 (2017).
33. Wei, N. et al. Wafer-scale fabrication of carbon-nanotube-based CMOS transistors and circuits with high thermal stability. *Nano Res.* **15**, 9875–9880 (2022).
34. Tang, J. et al. Flexible CMOS integrated circuits based on carbon nanotubes with sub-10 ns stage delays. *Nat. Electron.* **1**, 191–196 (2018).
35. Wang, Y. et al. Sub–180-nanometer-thick ultraconformable high-performance carbon nanotube–based dual-gate transistors and differential amplifiers. *Sci. Adv.* **10**, eadq6022 (2024).
36. Chen, B. et al. Highly uniform carbon nanotube field-effect transistors and medium scale integrated circuits. *Nano Lett.* **16**, 5120–5128 (2016).
37. Zhang, Z. et al. Doping-free fabrication of carbon nanotube based ballistic CMOS devices and circuits. *Nano Lett.* **7**, 3603–3607 (2007).
38. Wang, H. et al. Tuning the threshold voltage of carbon nanotube transistors by n-type molecular doping for robust and flexible complementary circuits. *Proc. Natl. Acad. Sci. USA* **111**, 4776–4781 (2014).
39. Lau, C., Srimani, T., Bishop, M. D., Hills, G. & Shulaker, M. M. Tunable n-Type Doping of Carbon Nanotubes through Engineered Atomic Layer Deposition HfO(X) Films. *ACS Nano* **12**, 10924–10931 (2018).
40. Ha, T. J. et al. Highly uniform and stable n-type carbon nanotube transistors by using positively charged silicon nitride thin films. *Nano Lett.* **15**, 392–397 (2015).
41. Tousignant, M. N., Ronnasi, B., Tischler, V., Lessard, B. H. N-Type single walled carbon nanotube thin film transistors using green tri-layer polymer dielectric.*Adv. Mater. Interfaces* **10**, 2370047 (2023).
42. Zhang, Y. et al. 3D Stackable CNTFET/RRAM 1T1R array with CNT CMOS peripheral circuits as BEOL buffer macro for monolithic 3D integration with analog RRAM-based computing-in-memory. In*2023 International Electron Devices Meeting (IEDM)*) (2023).
43. Kanhaiya, P. S., Lau, C., Hills, G., Bishop, M. D. & Shulaker, M. M. Carbon nanotube-based CMOS SRAM: 1 kbit 6 T SRAM arrays and 10 T SRAM cells. *IEEE Trans. Electron Dev.* **66**, 5375–5380 (2019).
44. Long, G. et al. Carbon nanotube-based flexible high-speed circuits with sub-nanosecond stage delays. *Nat. Commun.* **13**, 6734 (2022).
45. Chen, H., Cao, Y., Zhang, J. & Zhou, C. Large-scale complementary macroelectronics using hybrid integration of carbon nanotubes and IGZO thin-film transistors. *Nat. Commun.* **5**, 4097 (2014).
46. Liu, L. et al. Carbon nanotube complementary gigahertz integrated circuits and their applications on wireless sensor interface systems. *ACS Nano* **13**, 2526–2535 (2019).
47. Lv, J., Shen, Z., Meng, D., Peng, L. M. & Qiu, C. High-performance dual-gate transistors based on aligned carbon nanotubes. *ACS Appl. Mater Interfaces* **16**, 58864–58871 (2024).
48. Cheng, Z. et al. How to report and benchmark emerging field-effect transistors. *Nat. Electron.* **5**, 416–423 (2022).
49. Cao, Q. et al. Medium-scale carbon nanotube thin-film integrated circuits on flexible plastic substrates. *Nature* **454**, 495–500 (2008).
50. Holmes-Siedle A., Adams L. *Handbook of Radiation Effects*. (Oxford University Press, 2002).
51. Gaillardin, M. et al. High tolerance to total ionizing dose of Ω-shaped gate field-effect transistors. *Appl. Phys. Lett.* **88**, 223511 (2006).
52. Colinge, J. P. et al. Radiation dose effects in trigate SOI MOS transistors. *IEEE Trans. Nuclear Sci.* **53**, 3237–3241 (2006).
53. Draper, B., Okandan, M. & Shaneyfelt, M. Radiation response of a gate-all-around silicon nano-wire transistor. *IEEE Trans. Nuclear Sci.* **56**, 3274–3279 (2009).
54. El Mamouni, F. et al. Fin-width dependence of ionizing radiation-Induced subthreshold-swing degradation in 100-nm-gate-length finFETs. *IEEE Trans. Nuclear Sci.* **56**, 3250–3255 (2009).
55. Paillet, P. et al. Total ionizing dose effects on deca-nanometer fully depleted SOI devices. *IEEE Trans. Nuclear Sci.* **52**, 2345–2352 (2005).
56. Luo, M. et al. Radiation-hard and repairable complementary metal-oxide-semiconductor circuits integrating n-type indium oxide and p-type carbon nanotube field-effect transistors. *ACS Appl. Mater Interfaces* **12**, 49963–49970 (2020).
57. McMorrow, J. J. et al. Radiation-hard complementary integrated circuits based on semiconducting single-walled carbon nanotubes. *ACS Nano* **11**, 2992–3000 (2017).
58. Wang, X. et al. Ultralow-power and radiation-tolerant complementary metal-oxide-semiconductor electronics utilizing enhancement-mode carbon nanotube transistors on paper substrates. *Adv Mater* **34**, e2204066 (2022).
59. Zhao, Y. et al. Radiation effects and radiation hardness solutions for single-walled carbon nanotube-based thin film transistors and logic devices. *Carbon* **108**, 363–371 (2016).
60. Cress, C. D., McMorrow, J. J., Robinson, J. T., Friedman, A. L., Landi, B. J. Radiation effects in single-walled carbon nanotube thin-film-transistors. *IEEE Trans. Nuclear Sci.***57**, 3040–3045 (2010).
61. https://physics.nist.gov/PhysRefData/XrayMassCoef/tab3.html.

62. https://www.engineeringtoolbox.com/emissivity-coefficients-d_447.html.
63. Jiang, K., Li, Q. & Fan, S. Spinning continuous carbon nanotube yarns. *Nature* **419**, 801–801 (2002).
64. Ma, Z., Han, J., Yao, S., Wang, S. & Peng, L.-M. Improving the performance and uniformity of carbon-nanotube-network-based photodiodes via yttrium oxide coating and decoating. *ACS Appl. Mater. Interfaces* **11**, 11736–11742 (2019).
65. Ortiz-Conde, A. et al. A review of recent MOSFET threshold voltage extraction methods. *Microelectron. Reliab.* **42**, 583–596 (2002).



## Acknowledgements

This work was supported by the National Natural Science Foundation of China (grants 52402167(K.Z.), T2394474(W.-S. Z.), T2394470(W.-S.Z.), 62371019(X.-Y.L.), T2394475(X.-Y.L.)), the National Key Research and Development Program of China (grants 2022YFB4400200(W.-S.Z.), and 2024YFA1210601(P.L.)), the Research Start-up Funds of Hangzhou International Innovation Institute of Beihang University (grant 2024KQ052(X.-Y.L.)), the Postdoctoral Fellowship Program of CPSF (grant GZC20233368(K.Z.)), the China Postdoctoral Science Foundation (grants 2024M764084(K.Z.), and 2025T181122(K.Z.)), the Fundamental Research Funds for the Central Universities (JKF-2025001724713(W.-S.Z.)), the Beijing Outstanding Young Scientist Program(W.-S.Z.), and National Key Laboratory of Science and Technology on Vacuum Electronics(P.L. and K.Z.). We thank Prof. Kaili Jiang (Tsinghua University) for proving the suspended CNTs, Wenxin Wang for technical assistance with CNT-films transfer, Xiao Bi for discussions on γ-ray irradiation processes, Jiangtao Wang, Yifan Liu, Xuze Fu, Yuanqi Wei, Guo Chen, and Zi Yuan for discussions on mechanism of irradiation.


## Author contributions

W.-S.Z. and L.-M.P. supervised the project. K.Z., H.-T.X., X.-Y.L., L.-M.P., and W.-S.Z. proposed the project. K.Z., N.-F.G., and H.-T.X. designed the experiments. N.-F.G. and K.Z. carried out the device fabrication. K.Z. and J.-B.Z. performed the irradiation experiments. K.Z. performed the electrical characterization and materials characterizations (SEM, TEM, AFM, XPS, and Raman). K.Z. growth and manipulation of suspended CNTs. L.-M.P., H.-T.X., K.Z., and Y.L. contributed to the device modeling and data analysis. K.Z., H.T.X., X.-Y.L., and L.-M.P. wrote the manuscript. J.-H.Z., D.-M.Z., P.L., and X.H.W. discussed the results and provided constructive comments on the manuscript.

## Competing interests

The authors declare no competing interests.

## Additional information

**Supplementary information** The online version contains supplementary material available at https://doi.org/10.1038/s41467-026-68673-0.

**Correspondence** and requests for materials should be addressed to Xiaoyang Lin, Haitao Xu or Lian-Mao Peng.

**Peer review information** *Nature Communications* thanks Daiming Tang and the other anonymous reviewer(s) for their contribution to the peer review of this work. A peer review file is available.

**Reprints and permissions information** is available at http://www.nature.com/reprints

**Publisher's note** Springer Nature remains neutral with regard to jurisdictional claims in published maps and institutional affiliations.

**Open Access** This article is licensed under a Creative Commons Attribution-NonCommercial-NoDerivatives 4.0 International License, which permits any non-commercial use, sharing, distribution and reproduction in any medium or format, as long as you give appropriate credit to the original author(s) and the source, provide a link to the Creative Commons licence, and indicate if you modified the licensed material. You do not have permission under this licence to share adapted material derived from this article or parts of it. The images or other third party material in this article are included in the article's Creative Commons licence, unless indicated otherwise in a credit line to the material. If material is not included in the article's Creative Commons licence and your intended use is not permitted by statutory regulation or exceeds the permitted use, you will need to obtain permission directly from the copyright holder. To view a copy of this licence, visit http://creativecommons.org/licenses/by-nc-nd/4.0/.

© The Author(s) 2026